



# Topology, dynamics, and control of a muscle-architected soft arm

Arman Tekinalp<sup>a</sup> , Noel Naughton<sup>b,1</sup> , Seung Hyun Kim<sup>a</sup> , Udit Halder<sup>c,2</sup> , Rhanor Gillette<sup>d</sup> , Prashant G. Mehta<sup>a,c</sup>, William Kier<sup>e</sup> , and Mattia Gazzola<sup>a,f,g,3</sup>

Affiliations are included on p. 11.

Edited by Daniel Goldman, Georgia Institute of Technology, Atlanta, GA; received December 5, 2023; accepted August 9, 2024, by Editorial Board Member Linda R. Petzold

Muscular hydrostats, such as octopus arms or elephant trunks, lack bones entirely, endowing them with exceptional dexterity and reconfigurability. Key to their unmatched ability to control nearly infinite degrees of freedom is the architecture into which muscle fibers are weaved. Their arrangement is, effectively, the instantiation of a sophisticated mechanical program that mediates, and likely facilitates, the control and realization of complex, dynamic morphological reconfigurations. Here, by combining medical imaging, biomechanical data, live behavioral experiments, and numerical simulations, an octopus-inspired arm made of ~200 continuous muscle groups is synthesized, exposing “mechanically intelligent” design and control principles broadly pertinent to dynamics and robotics. Such principles are mathematically understood in terms of storage, transport, and conversion of topological quantities, effected into complex 3D motions via simple muscle activation templates. These are in turn composed into higher-level control strategies that, compounded by the arm’s compliance, are demonstrated across challenging manipulation tasks, revealing surprising simplicity and robustness.

biomechanics | Cosserat rods | mechanical intelligence | muscular hydrostats | computational mechanics

By forgoing hard skeletal support in favor of three-dimensional, densely packed fiber structures, muscular hydrostats bypass rigid kinematic constraints to achieve unparalleled dexterity and reconfigurability (1, 2). It is thus perhaps not surprising that these solutions have independently evolved across taxa and environments (Fig. 1), from the flickering or prehensile tongues of lizards (1) and giraffes (3) to the nimble trunks of elephants (4) or arms of octopuses (1), long fascinating biologists, mathematicians, and engineers alike. Key to these organs’ dexterity are the architectural motifs into which muscle fibers are weaved and connected together. Indeed, muscular connectivity encodes “mechanically intelligent” programs that couple muscle groups’ dynamics and translate simple 1D contractions into complex 3D arm deformations, possibly relieving the nervous system of taxing computations (5–7). Despite much interest and broad technological implications (8–14), distilling design and control principles from these intricate organs has proved challenging.

Kinematic studies of animal tentacles (15), arms (16–19), tongues (20, 21), and trunks (22–24) have provided useful characterizations but cannot fully elucidate the relationship between control, muscle activation, and dynamics. Initial insight into these relations has been derived from electromyography recordings in octopus arms (25–28), illustrating how simple templates of electrical activity, consisting of traveling and colliding waves, underlie bend propagation (25, 26) and joint formation during planar fetching motions (27, 28). Nonetheless, full spatial and temporal activation patterns at the individual muscle level, particularly important for decoding the organization of 3D movements, remain inaccessible. Robophysical approaches, despite tremendous progress (29–42), have also struggled to make inroads, stymied by the lack of advanced materials (43) able to replicate the architecture and performance of natural muscular hydrostats. Within this context, *in silico* approaches can complement *in vivo* and robotic ones, allowing us to mathematically abstract, flexibly alter, and computationally explore the functioning of these systems. However, notwithstanding significant efforts (44–60), no modeling description has yet reached the maturity necessary to capture the extraordinary complexity of muscular hydrostats.

Here, by employing histological assays, diffusion MRI tractography, biomechanical data, and live behavioral experiments, we numerically instantiate an octopus-inspired arm out of soft, active, three-dimensionally intertwined muscle fibers. This model allows for the selective recruitment of specific muscle groups (individually or in concert, globally

## Significance

Muscular hydrostats such as octopus arms or elephant trunks are exceedingly deft and nimble, thanks to their boneless nature and intricate architecture. How effective control over these complex structures is achieved, remains an open question. Here, we combine medical imaging, biomechanics, and live behavioral experiments into an octopus arm model made of nearly 200 muscle groups, to expose simplifying “mechanically intelligent” design and control principles. By relating topology to muscle dynamics, we show how anatomical connectivity and tissue compliance naturally produce complex arm reconfigurations out of simple yet robust actuation patterns. While derived for the octopus, distilled insights, topological analysis, and modeling approach are broadly significant, not only to other muscular hydrostats, but also to robotics, dynamics, and control.

The authors declare no competing interest.

This article is a PNAS Direct Submission. D.G. is a guest editor invited by the Editorial Board.

Copyright © 2024 the Author(s). Published by PNAS. This article is distributed under Creative Commons Attribution-NonCommercial-NoDerivatives License 4.0 (CC BY-NC-ND).

<sup>1</sup>Present address: Department of Mechanical Engineering Virginia Tech Blacksburg, VA 24061.

<sup>2</sup>Present address: Department of Mechanical Engineering, University of South Florida, Tampa, FL 33620.

<sup>3</sup>To whom correspondence may be addressed. Email: mgazzola@illinois.edu.

This article contains supporting information online at <https://www.pnas.org/lookup/suppl/doi:10.1073/pnas.2318769121/-DCSupplemental>.

Published October 1, 2024.

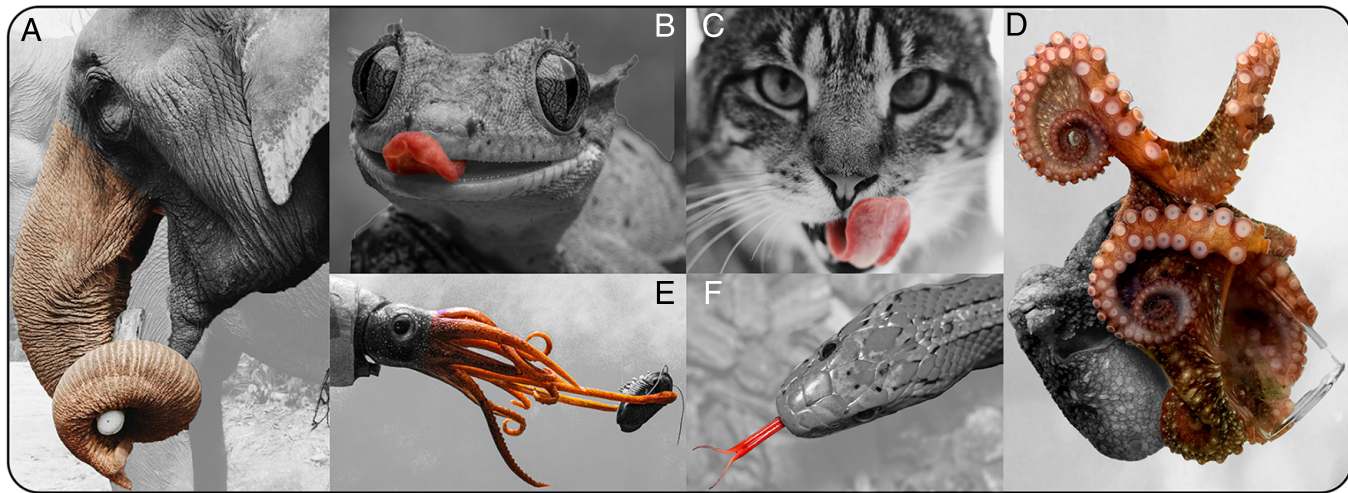


**Fig. 1.** Muscular hydrostats are widespread in nature. (A) Elephant trunks [Image credit: Irene Grace Tolentino (photographer)], (B) gecko tongues [Image credit: Peter Law (photographer)], (C) cat tongues [Image credit: Megan McClain (photographer)], (D) octopus arms, (E) squid arms and tentacles [Image credit: Meressa Chartrand (photographer)], and (F) snake tongues [Image credit: Zdeněk Macháček (photographer)] are all examples of muscular hydrostats that have independently evolved to enable a variety of deformations and functions.

or locally) to examine how their structural arrangement contributes to complex motions (16), and is used here to decode principles of design and control, revealing surprising simplicity and robustness. This level of inspection cannot be attained with existing single-rod arm representations (44–60). Indeed, in such cases, the arm's structure, heterogeneity, and anisotropy is foregone, and muscular activity is lumped into cumulative (and often arbitrary) torque/force functions applied to the rod, creating a disconnect with the three-dimensionally organized actuators that are in fact responsible for these cumulative loads in the first place.

Using our model instead, templates of muscle (co)activations are related to the storage, conversion, transport, and release of three topological/geometric descriptors which, mediated by the arm's compliance, dynamically unfold into complex morphological reconfigurations. The intuitive composition of such templates allows orchestrating high-level tasks, whereby, for example, an arm can squeeze through a crevice with its suckers exposed outward for sensing, reach for an object on the other side, realign the suckers inward to grasp it, manipulate it, and retrieve it. Further compounding the robustness of this approach, the interplay between the conformable arm and solid interfaces is found to rectify imprecise control, allowing the arm to passively accommodate obstacles and objects of different geometries without changes in muscle activation.

By focusing on general principles of soft arm control, rather than animal-specific behaviors, this work goes beyond the octopus instance that inspires it. Indeed, this study identifies design and control strategies broadly rooted in topology, geometry, and mechanics, with implications in biology, dynamics, and robotics. Further, it significantly advances simulating from medical imaging, with opportunities in biomechanics, health, and medicine (61).

**Modeling of an Octopus-Inspired Soft Arm.** Of all muscular hydrostats, octopus arms exhibit perhaps the greatest capacity for dexterous manipulation, making them natural candidates for investigating the nexus between architecture, actuation, and control in soft systems. We then consider an octopus-inspired arm and model its internal organization through assemblies of Cosserat rods (Fig. 2*A*, *Materials and Methods*). These are

one-dimensional elastic fibers that can undergo at every (circular) cross-section all six modes of deformation (bending, twisting, shearing, and stretching), and thus continuously deform in 3D space while conserving volume (63, 64). Cosserat rods provide a convenient mathematical representation in the present context: they naturally map onto muscle fibers and groups, can actively contract at any location according to prescribed force-length relations, and can be connected together (via appropriate boundary conditions) into complex structures (65). They are thus ideally suited to capture the heterogeneous and anisotropic nature of muscular hydrostats, together with their internal loads' distributed generation and transmission. Here, the Cosserat rod equations (*Materials and Methods*, *SI Appendix*) are numerically solved using the open software Elastica (66), whose accuracy and utility has been extensively demonstrated through rigorous benchmarks (63, 67), quantitative simulations of animal locomotion (65, 68, 69), plant dynamics (70), fibrous metamaterials (71, 72), and for the design and control of artificial (49, 54–56, 73) as well as biohybrid (65, 74, 75) soft robots.

To instantiate our arm *in silico*, octopus geometric and biomechanical properties are incorporated within our representation. We begin by considering histological cross-sections of *O. rubescens* to highlight the arm's main structural elements (Fig. 2 *A* and *B*): a passive axial nerve cord surrounded by longitudinal, transverse, and oblique muscle groups (76, 77).

The nerve cord (ANC) and longitudinal muscles (LM) span the full length of the arm and run parallel to it, with the nerve cord centered along the midline and the longitudinal muscles located off-axis (Fig. 2 *A* and *B*). When all longitudinal muscles contract, the arm shortens on account of the resulting axially compressive forces (Fig. 2 *I-1*). If instead longitudinal muscles are selectively activated on one side of the arm, contractile forces result in distributed couples due to their off-axis alignment, producing bending (Fig. 2 *I-2*). To morphologically and functionally recapitulate this structure, the nerve cord is modeled as a single passive central rod (Fig. 2*A*, pink) while longitudinal muscles are represented by eight surrounding active rods (Fig. 2*A*, green). This number (eight) stems from using rods of circular cross-section with diameters determined to approximate natural proportions (ANC occupies ~10% of the arm cross-section, ~50% for LM; see *SI Appendix*). Biomechanically, the contractile and

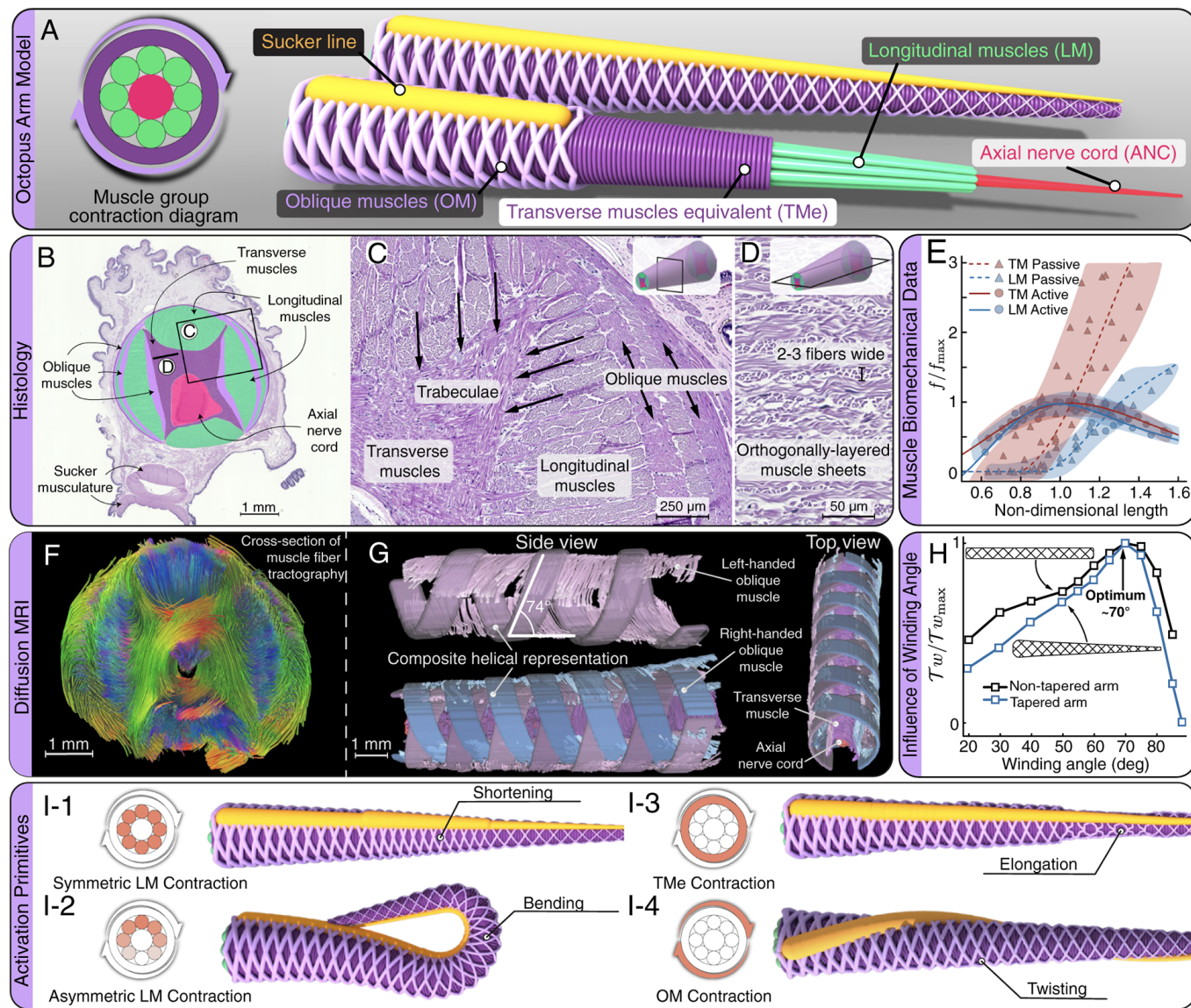


**Fig. 2.** Computational modeling of an octopus arm from histological, biomechanical, and diffusion MRI tractography data. (A) Cosserat rods are assembled to functionally recapitulate the octopus arm architecture. (B) Transverse slice of *Octopus rubescens* arm (H&E stain) with key muscle groups and anatomical features labeled. Histology Insets show: (C) infiltration of trabeculae through the longitudinal muscles. Trabeculae act as force transmission pathways to the arm's outer layers, allowing transverse muscles to radially squeeze the arm. (D) Frontal slice of transverse muscles showing alternating arrays of orthogonal fibers, enabling transversely isotropic and axially decoupled stress generation. (E) Force-length relationships of longitudinal and transverse muscles (solid lines) fitted to experimental data of an *Octopus vulgaris* reported by Zullo et al. (62). (F) Diffusion MRI tractography of *O. rubescens* arm showing 3D muscle-fiber arrangement. (G) Segmentation of muscle groups allows identification of key morphological features for inclusion in our model such as the winding angle of the oblique muscle (OM) layers. (H) Effect of OM winding angle on twisting performance for both nontapered and tapered arms. Simulations show that maximum twist is generated at a winding angle of 70°. (I) Motion primitives arise from individual muscle group contractions: shortening (symmetric LM), bending (asymmetric LM), elongation (TMe), and twisting (OM).

elastic behavior of longitudinal muscles, i.e., their characteristic active/pассив stress-strain relationships (Fig. 2E), are based on muscle-specific measurements of *O. vulgaris* by Zullo et al. (62). Incorporating muscle specificity is critical to capture the octopus' reconfigurability, where longitudinal muscles operate over a much wider length-range than transverse muscles (62, 78, 79). Finally, the passive response of the nerve cord is modeled as for LM.

Transverse muscles (TM) are anatomically located between, and orthogonal to, the nerve cord and longitudinal muscles (Fig. 2 A and B). Their activation radially compresses the arm, causing it to extend axially due to the tissue's near-incompressibility (Fig. 2 I-3). The cross-sectional enlargement of Fig. 2B reveals the intricate microstructure that enables this

function. Emanating from the transverse muscles, thin muscular strips (trabeculae) infiltrate through the longitudinal muscles, reaching into the arm's outer layers (Fig. 2C), forming a dense fan of tethers. These transmit transverse muscle contraction forces to the arm's periphery, which in turn redistributes them as radial compressions over the cross-section. Further, transverse muscles are organized in independent sheets (two to three fibers thick), each orthogonal to the arm's axis and alternating perpendicular fiber-alignments (frontal slice of Fig. 2D). This orthogonal packing allows individual sheets to approximately slip past each other during contractions, generating both finely localized and transversely isotropic compression forces without entanglement. We recapitulate the effective mechanics of this axially decoupled, interdigitated microstructure via a concatenated series of

contractile rings (TMe—as in TM equivalent—in Fig. 2A, dark purple) enveloping the LM. This choice simplifies the numerical treatment while capturing the axially localized, cross-sectional squeezing that results from the combined effect of inner TM, trabeculae, and outer layer. Support for this modeling approach (beyond the histological data of Fig. 2C) is further provided by the anatomy of lizard (1) and snake (80) tongues (also muscular hydrostats), where circumferential muscles that are functionally equivalent to the octopus' transverse muscles (1), are indeed located at the periphery of the organs' cross-section (*SI Appendix*). Concurrently, we enhance the Cosserat formalism to capture the effect of intramuscular pressure. This is generated by transverse contractions and is responsible for the arm elongation due to incompressibility. Our Cosserat rod formulation (63), which already naturally conserves volume (incompressibility), is then paired with a pressure model that accounts for all local forces radially perpendicular to any rod at every cross-section. The model is detailed in *Materials and Methods*, with quantitative validations against squid tentacle strike experiments (44) reported in *SI Appendix*. Finally, ring (TMe) dimensions are based on the relative cross-sectional area occupied by the transverse muscles (~20%), while their contractile and elastic properties reflect data from Zullo et al. (62) (Fig. 2E).

Oblique muscles (OMs) are helically arranged around the arm and, upon contraction, twist it (Fig. 2 I–4). To visualize this nonplanar architecture, we performed high-resolution, diffusion-weighted MRI (dMRI) of an *O. rubescens* arm using a high-field 9.4 T scanner (*Materials and Methods*). dMRI measures the direction-dependent diffusion of water in material samples (81). In fibrous tissue, water molecules preferentially diffuse along fibers, thus encoding structural information into the dMRI signal. Tractography can then be employed to directly extract fibers' spatial organization, synthesizing the three-dimensional architecture of the tissue (82). Applied here to an octopus arm, dMRI tractography reveals its volumetric, muscular organization (Fig. 2F and G), expanding upon the architectural motifs gleaned from local, two-dimensional histology and further guiding our modeling intuition (all imaging data are openly distributed; see Data Access statement). The oblique musculature is organized into three layers, external, medial, and internal, on both sides of the arm. Consistent with previously reported microscopy (76), the handedness of fibers alternates by layer and is opposite to its contralateral pair (i.e., the external and internal layers on one side have the same handedness as the medial layer on the opposite side). Similarly handed layers form a composite helical system (Fig. 2G), whereby forces produced by contractions on one side of the arm are transmitted, through the connective tissue found at the top (aboral) and bottom (oral) of the arm, to the opposite side, enabling twisting motions. Thus, mechanically, this infrastructure is approximately equivalent to a sheath of helically wound continuous fibers, and we model it as two sets of four opposite-handed helical strands (R-OM and L-OM, Fig. 2A, bright purple) wrapping along the full length of the arm at a 74° angle from the base, to match tractography measurements. Notably, we find in simulations (Fig. 2H) that this winding angle (~70°) maximizes twist generation upon OM contraction, providing a potential mechanistic rationale for the evolution of this particular arrangement, as well as a useful design guideline for engineers (*SI Appendix*). The employed number of rods (eight) approximates the OM cross-sectional area proportions (~20%). Biomechanical force-length relationships for OMs do not exist, and we use the LM data of Fig. 2E.

Fully assembled, our model arm consists of 197 rods (1 ANC, 8 LM, 4 R-OM + 4 L-OM, and 180 TMe rods) and, in

keeping with measurements of *O. rubescens* (54), has a length of 20 cm, a diameter at the base of 24 mm, and a tapering angle of 87°. Rods are bound together via distributed boundary conditions that approximate the passive elastic effects of the connective tissue (76) (*SI Appendix*). While octopus muscles are enervated by three types of synaptic inputs (84), for simplicity and generality we model activations as a single input that produces localized, continuously graded tonic contractions. Thus, each muscular rod can contract at any position along its length, generating axially compressive forces that are mechanically translated by the arm's architecture into 3D dynamic motions. We note that among the 300 living species of octopus (85) a level of geometric diversity exists (86), particularly regarding arm lengths, from 1 cm (*Octopus wolfi*) to 3 m (*Enteroctopus dofleini*), but also taper angles, from ~80° (*Eledone cirrhosa*) to ~90° (*Thaumoctopus mimicus*). However, anatomically, octopus arms exhibit remarkable consistency (76, 87), rendering our model well-suited to distill broad, cross-species mechanical and control principles. From this model, basic motion primitives conserved across octopuses (16), such as bending (asymmetric LM contraction), twisting (OM), shortening (symmetric LM contraction), and elongation (TMe) naturally arise (Fig. 2I). Arm kinematics can then be connected to the muscle activations that beget them, setting the stage for exploring their composition into complex behaviors.

**A Topological View Informed by Live Octopus Experiments.** Analogous to the complexity of real octopus arms, our model—with nearly 200 rods bundled together, each able to continuously contract and elastically deform—is highly nonlinear and characterized by a vast number of degrees of freedom. Controlling such a system is a daunting task.

To simplify the problem and gain a broader perspective unobscured by the arm's specific details, we adopt a topological and geometric view. We start by considering the arm's centerline, the blue directed curve of Fig. 3B with edges highlighted in yellow and pink, to understand its kinematic reconfiguration through the descriptors link ( $\mathcal{L}k$ ), writhe ( $Wr$ ), and twist ( $Tw$ ). This is a mathematical representation long employed in biology to characterize the supercoiling morphology of DNA (83, 88). Link ( $\mathcal{L}k$ ), a topological invariant, is the oriented crossing number (or Gauss linking integral) of the centerline and one of its edges (pink auxiliary curve), averaged over all projections. Practically, link quantifies how much the two curves wind around each other. Writhe ( $Wr$ ) is a global geometric quantity equivalent to the link of the centerline with itself. Essentially, it captures how much the curve bends and coils but does not account for the orientation of the edges. Twist ( $Tw$ ), also a geometric quantity, accounts for this orientation, measuring the total rotation of the auxiliary pink curve about the centerline's tangent. Critically, these quantities are related through the Calugareanu–Fuller–White (CFW) theorem (83, 89)

$$\mathcal{L}k = Wr + Tw, \quad [1]$$

allowing us to understand arm reconfigurations in terms of injection, storage, and interconversion of only three quantities. For the purpose of illustration, in Fig. 3B, a set of helices of constant arc-length, but varying pitch angle (0° to 90°), are geometrically constructed (no mechanics involved) under the constraint of orientations (tangents, normal, binormals) matching at their ends. This constraint renders the open, helical blue curve equivalent to a closed one, in that link is exactly conserved (90) (*SI Appendix*). Initially, the straight centerline

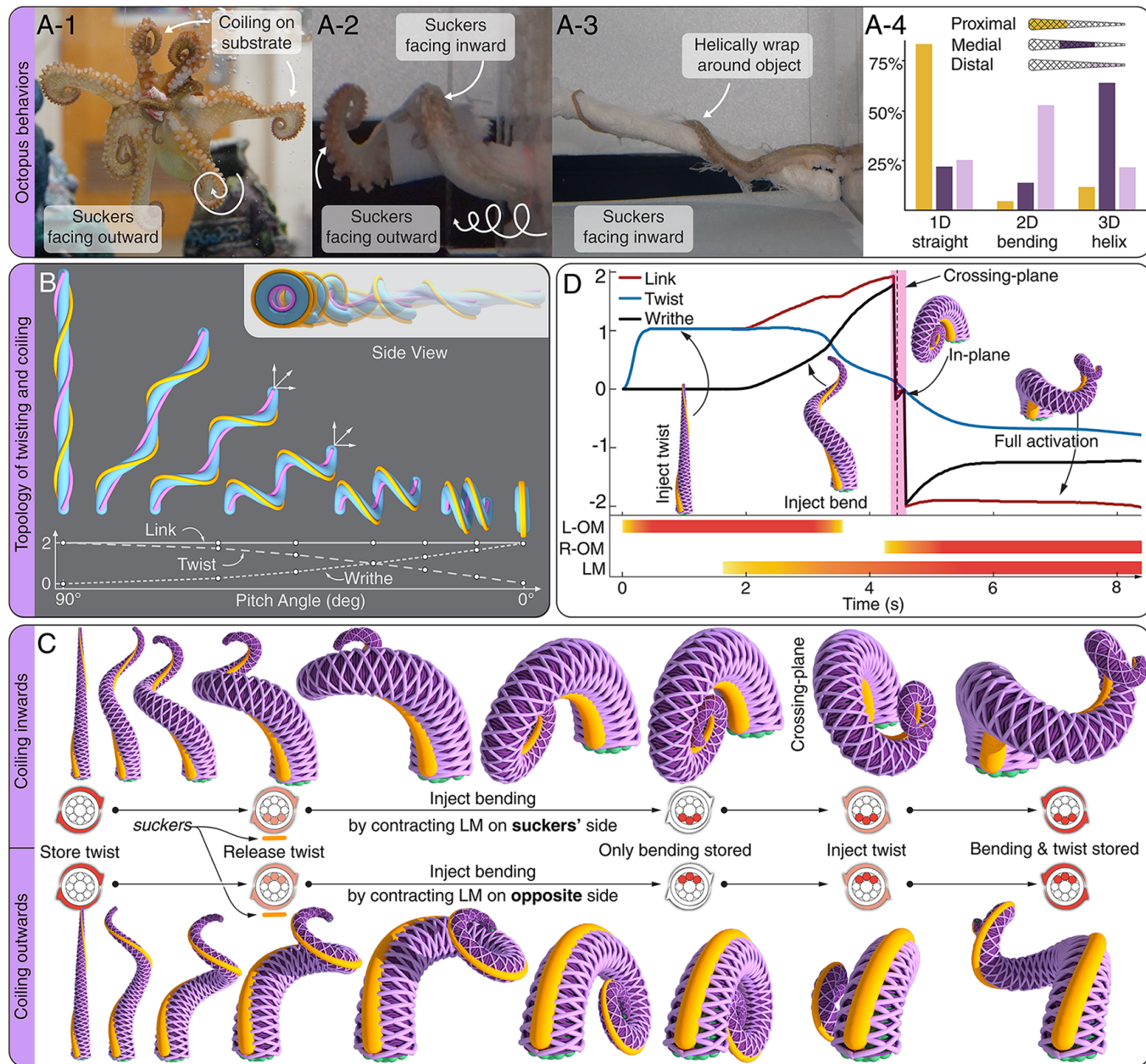


**Fig. 3.** Topological and dynamic interpretation of an octopus arm. (A) Example images of an octopus coiling its arms against a substrate (A—1) and forming 3D helical structures (A—2 and A—3) during object grasping. (A—4) Video analysis in controlled conditions (see examples in Movie S1) reveals the distribution of an octopus arm's deformation modes during object grasping and manipulation. Statistical analysis of the distribution of deformations is provided in SI Appendix. (B) Illustration of CFW Theorem at work: a single directed curve (blue) and its associated auxiliary curves (yellow/pink) are twisted twice ( $\mathcal{T}w = 2$ ), injecting constant link ( $\mathcal{L}k = 2$ ). As pitch angle decreases ( $90^\circ \rightarrow 0^\circ$ ), twist is converted into writhe, reconfiguring the rod's morphology from straight ( $\mathcal{T}w = 2, \mathcal{W}r = 0$ ) to helical to planar spiraling ( $\mathcal{T}w \rightarrow 0, \mathcal{W}r \rightarrow 2$ ). (C) Dynamic deformation of a helically coiling arm. A straight arm stores twist by contracting its L-OM and then forms helices by additionally contracting LM before folding into a spiral after relaxing L-OM. Reinjecting twist (R-OM), while keeping LM contracted, extends the arm telescopically and perpendicularly. (Top row) Contraction of LM adjacent to the suckers aligns them inward. (Bottom row) LM activation on the opposite side aligns suckers outward (Movie S2). (D) Evolution of  $\mathcal{L}k$ ,  $\mathcal{W}r$ , and  $\mathcal{T}w$  during the reconfiguration of (C, top row). Pink shading denotes the transition plane where the arm crosses through itself twice (because of its two loops), causing  $\mathcal{W}r$  and  $\mathcal{L}k$  to decrease by four (83).

( $\mathcal{W}r = 0$ ) is twisted two full rotations ( $\mathcal{T}w = 2$ ), injecting and permanently storing  $\mathcal{L}k = 2$ . As the helical pitch increases, 3D coils begin to manifest. Coils are associated with writhe ( $\mathcal{W}r \uparrow$ ), forcing the centerline to untwist ( $\mathcal{T}w \downarrow$ ) since link cannot vary. Thus, as twist is converted into writhe, the helix axially contracts, until no twist is left ( $\mathcal{T}w \rightarrow 0$ ), only writhe remains ( $\mathcal{W}r \rightarrow 2$ ), and the centerline approaches a planar coil.

While illustrative of the CFW theorem, this reconfiguration sequence is also a minimal abstraction of a broad class of

octopus behaviors (91–96). Indeed, planar coiling is commonly encountered in arms at rest or attached to a substrate (Fig. 3 A-1). To and from these configurations, arms often fold and unfold in helical fashion, over the full extent or a section of the arm, particularly when engaging with objects. We verify and quantify this via controlled behavioral experiments involving *O. rubescens* interacting with different objects (Fig. 3 A and Movie S1). Video analysis (Fig. 3 A-4, SI Appendix) reveals how proximal and distal sections primarily employ 1D (straight arm) and 2D (planar

bend/coil) configurations, respectively, with suckers typically exposed outward (Fig. 3 A-1 and 2). However, the medial section, where object engagement typically occurs (97), systematically employs helices to orient the suckers inward toward the substrate, wrap around it, and manipulate it (Fig. 3 A-2 and 3).

**Topological Control Via Uniform Muscle Actuation.** The above topological view compactly describes morphological changes from a purely kinematic standpoint, i.e., it does not provide any information relative to the mechanics at play. Thus, to distill potential actuation and control strategies underlying 3D arm manipulations, we connect topology to muscle dynamics. We first note that  $\mathcal{L}k$ ,  $\mathcal{W}r$ , and  $\mathcal{T}w$  are all global quantities, suggesting that global (i.e., uniform) muscle contractions over the full arm (or a section) may suffice to realize basic 3D behaviors. Second, since  $\mathcal{L}k$ ,  $\mathcal{W}r$ , and  $\mathcal{T}w$  are related through Eq. 1, only two of them need to be controlled, with  $\mathcal{W}r$  and  $\mathcal{T}w$  intuitive candidates because, unlike  $\mathcal{L}k$ , they are geometric descriptors that can be associated with the activity of specific muscle groups. Indeed, oblique muscles mediate  $\mathcal{T}w$ , while longitudinal muscles are associated with the manipulation of  $\mathcal{W}r$  through bending.

The utility and simplicity of this perspective for control is demonstrated in Fig. 3 C, Top/Left and Movie S2, where we consider the muscle actuations necessary to coil an initially at rest, straight octopus arm ( $\mathcal{L}k = \mathcal{W}r = \mathcal{T}w = 0$ ) into a helix before folding it into a spiral, following the purely geometric example of Fig. 3B. To dynamically realize this motion, we first uniformly contract the left-handed oblique muscles to inject twist ( $\mathcal{T}w = 1$ ), thus storing link ( $\mathcal{L}k = 1$ ) as a degenerate loop collapsed along the arm's midline. Subsequently, we unfold this loop into a helix by introducing  $\mathcal{W}r$  via the uniform contraction of longitudinal muscles on one side of the arm. Unlike the curve of Fig. 3B, here the tip orientation of the arm is free, allowing link to increase in response to longitudinal contractions. This manifests in the gradual appearance of a second coil as link approaches  $\mathcal{L}k = 2$ . Based on Fig. 3B, folding the newly formed helix into a spiral requires converting stored twist into writhe. To do so, we relax the oblique muscles (while keeping LM contracted), releasing twist into writhe (note faster growth rate in Fig. 3D), until a spiral ( $\mathcal{W}r = \mathcal{L}k = 2$ ) is obtained.

From here, we consider the arm's telescopic extension in the orthogonal direction (Fig. 3 C, Top/Right, Movie S2). First, we note that as the arm crosses the spiral plane, its equivalent knot passes through itself twice, causing writhe and link to decrease by four (83) (discontinuity in Fig. 3D), with the handedness (sign) of  $\mathcal{T}w$  switching from positive to negative. Second, as long as the LM (the strongest group) remain fully contracted, we expect the arm tip to approximately maintain its tangent, thus approaching the boundary condition of Fig. 3B. This implies a constant  $\mathcal{L}k \approx -2$  (SI Appendix), which we numerically confirm (Fig. 3D) and exploit to force twist to increase (in magnitude) at the expense of writhe (Eq. 1) by contracting R-OM, thus unfolding the helix (Fig. 3 C, Top/Right).

This demonstration illustrates how as few as two degrees of freedom (uniform contraction of LM, L/R-OM) are sufficient to orchestrate 3D stereotyped octopus behaviors. This drastic reduction in the control problem's dimensionality is an example of mechanical intelligence at play, whereby nonlinear couplings arising from the arm's compliance and anatomical design take care of producing complex morphological transitions out of uniform, global contractions. In this context, the topology–dynamics connection established here allows us to understand and exploit the arm infrastructure to our advantage.

**Sucker Alignment.** Octopuses utilize their suckers for environmental sensing and object grasping. Their alignment is a non-trivial control problem, particularly during 3D motions. Indeed, it requires carefully matching the rotation of the arm (twist) with its curvature (bending), as the arm itself is morphing into shape. Our topological interpretation allows us to understand how this task can be vastly simplified by the arm architecture.

Suckers and longitudinal muscles run parallel to the arm axis at a radial offset, and thus they represent physical auxiliary curves of fixed relative positions around the axis. As a consequence, their common axial rotation is determined by the oblique muscles through the injection of  $\mathcal{T}w$  (Fig. 3C, leftmost side). When twist is present in the system, the introduction of  $\mathcal{W}r$  through one-sided activations of LM morphs the arm into 3D shape (Fig. 3 B and D). Now, because of the fixed relative position and common orientation of the active LM and suckers, the extent to which the latter are exposed outward (convex side) or tucked inward (concave side, Fig. 3 A–2) is finally governed by which set of LM is activated. Indeed, as illustrated in Fig. 3C, top row, the actuation of the LM on the suckers' (oral) side causes the suckers to face inward, a useful feature during grasping. It is instead sufficient to contract the opposite set of LM (aboral side) to expose all suckers outward (for sensing), while retaining the same arm morphology (Fig. 3C, bottom row). Any other degree of suckers exposure can be attained by using the intermediate LM located between the oral and aboral sides.

This mechanism is critically enabled by the coactivation of both oblique and longitudinal muscles. Indeed, while LM alone can form any 3D axial shape by controlling writhe, they cannot (fully) determine the orientation of the auxiliary curves, which requires additional command over twist (OM). In SI Appendix, we show how LM alone can form helices via local, staggered, clockwise activations around the arm axis and along its length. However, this strategy is significantly more complex than the one of Fig. 3C and at the same time it forgoes control of the suckers, because their location relative to the clockwise contracting LM keeps varying along the arm (SI Appendix). Thus, the presence of oblique muscles within the arm structure simplifies both 3D reconfigurations and sucker alignment, a mechanically intelligent design that potentially justifies their evolutionary emergence.

We conclude by emphasizing that while the exact muscle activations the octopus employs remain unknown, our model compactly recapitulates a range of observations (Movie S7), providing hypotheses and insights rooted in mechanics and directly applicable to robotics and control.

**Geometric Transport Via Waves of Muscle Actuation.** Next, we augment uniform activation strategies with the transport of localized contractions along the arm. We are inspired by planar bend propagations in reaching motions (98). These motions have been particularly well characterized, through EMG recordings (25, 26), kinematic data (17), and dynamic modeling (18, 47, 55), converging on the hypothesis that bends are formed and transported by stiffening wavefronts of longitudinal and transverse muscle cocontractions. When a similar traveling wavefront ( $\mathcal{L}$ ) is tested in our arm, the model recapitulates bend propagation behaviors both qualitatively and quantitatively (Fig. 4A and SI Appendix), matching experimentally observed bend velocities (25, 98), thus further validating our approach. We note that simple muscle relaxation (from the initial bent configuration, Fig. 4A) is insufficient to achieve experimentally observed bend curvature and speed profiles. Indeed, the spatiotemporal scales of the arm's passive unfolding are dictated by its stiffness, which is low, leading to slow motions and poor localization

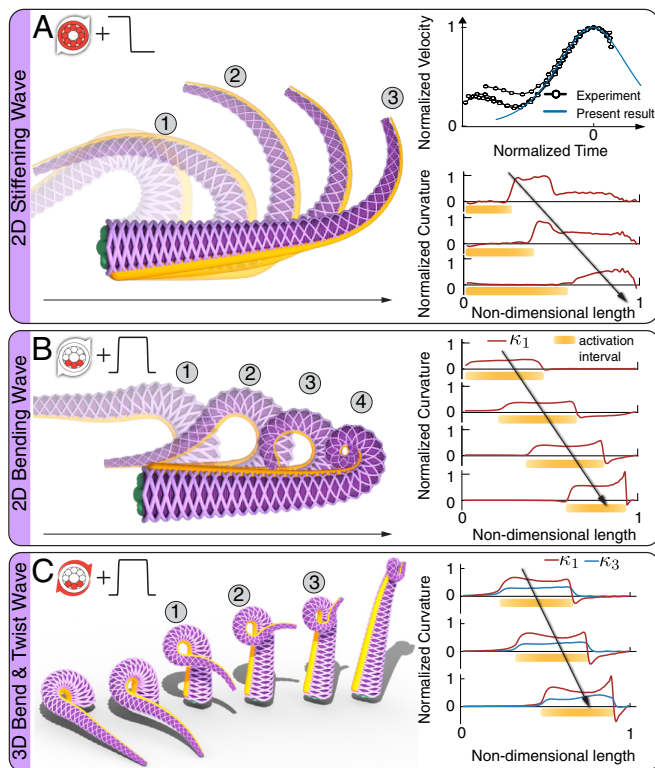


**Fig. 4.** Active geometric transport. (A) A stiffening wavefront ( $\text{J}_\perp$ ) generates a reaching motion by propagating a bend ( $\kappa_1$ ) along the arm (activation details in *SI Appendix*). Simulations replicate both the peak bend velocity (30 cm/s) and normalized bend velocity profile (*SI Appendix*) of experiments by Gutfreund et al. (25, 98). (B) A localized primitive is injected into the arm at its base and transported by a pulse ( $\text{J}_\perp$ ) of LM muscle activation (details in *SI Appendix*). The bending ( $\kappa_1$ ) profile shows the curvature packet transport in relation with LM activations. (C) Generalization of kernel activation and transport to 3D. Example of pulse ( $\text{J}_\perp$ ) of LM (bend) and OM (twist) activations (details in *SI Appendix*) and the resulting traveling curvature packets ( $\kappa_1, \kappa_3$ ). Initial arm configurations are achieved via muscle preactivations as detailed in *SI Appendix*. All motions are available in Movie S3.

(*SI Appendix*). Muscle activations then offer the opportunity to modify the arm's stiffness, thus modulating its passive baseline motion, suggesting potential control generalizations (99).

Indeed, moving beyond the octopus to broader issues of robotic actuation and control, the stiffening wave mechanism can be extended to generic muscle activation kernels. These are defined as spatially compact sets of muscle actuations that result in localized reconfigurations of the arm. Within this framework, we can revisit planar bend propagation as a traveling pulse ( $\text{J}_\perp$ ) of one-sided LM contractions to inject local curvature. Fig. 4B illustrates how this strategy allows the formation and transport of a tightening spiral which, as we will see later, can be used for object displacement. This approach can be readily generalized to 3D local structures, enhancing manipulation and reconfiguration abilities. In Fig. 4C, we inject a pulse ( $\text{J}_\perp$ ) of bending and twist at the base of the arm, via the cocontraction of LM and OM. As the pulse propagates along the arm, a localized corkscrew structure is seen to form, translate, and tighten.

In both cases, as the activation kernel travels past an arm segment, its passive elastic stiffness causes the segment to straighten. This mechanical response eliminates the need for additional muscle activations to rectify the deformation induced by the kernel, intelligently simplifying control and supporting reaching motions. Thus, through material selection (in robotics) or muscle/actuator coactivations (in both biology and robotics)

the extent to which passive elastic responses can be repurposed and leveraged toward desired motion tasks, can be controlled.

**Grasping, Manipulation, and Interfacial Interactions.** The injection and transport of actuation kernels, together with uniform templates, provide a general framework to understand grasping and manipulation in soft arms, whether natural or artificial.

We start by considering the grasping of a cylindrical post, as illustrated in Fig. 5A. To firmly grasp the object, the arm must form one or more coils around it. Geometrically, this implies  $|\mathcal{W}r| > 1$ , however, writhe alone is insufficient to ensure grasping, as the coil must be correctly oriented to encompass the object. We achieve this by revisiting the helix formation process of Fig. 3. By injecting localized twist (via R-OM contraction) into the proximal half of the arm, we orient the suckers toward the target, before contracting the longitudinal muscles on the suckers' side using a wavefront ( $\text{J}_\perp$ ) of activation (Fig. 5B). This causes the arm to dynamically conform around the object while aligning the suckers inward. The use of a muscle contraction wave is found to be significantly more robust than a uniform activation strategy. Indeed, a wave allows the arm to progressively wind around the post without intersecting it, while uniform actuations cause the arm to coil too early, bringing the distal end into contact, thus preventing successful grasping (*SI Appendix*).

To further demonstrate the reliability of the chosen approach, we test the ability of the exact same muscle activation sequence to deal with objects of different size (Fig. 5C), shape, and orientation (Fig. 5E). We exploit the fact that it is the obstacle's presence that passively informs and modulates the arm's morphology, as it complies and conforms to the presented target. This is another instance where mechanical intelligence is found to simplify and robustify control, leading to successful grasping across scenarios (Fig. 5 C–E). Confirming our geometric intuition, writhe decreases as the obstacle's circumference increases and, for  $|\mathcal{W}r| \lesssim 1$ , we begin to observe grasping failure, with the arm's distal end slipping off the obstacle (Fig. 5D). While octopuses supplement grasping with their suckers to securely attach to the substrate (97), here we do not explicitly include this effect. However, we do consider friction (both static and kinetic) and in *SI Appendix* show how this affects the onset of slipping, with low friction causing grasping failure. Overall, our activation strategy compactly and robustly abstracts a generic grasping kernel translatable to soft robotic arms, while remaining flexible enough to incorporate additional feedbacks. For example, interfacial forces may be modulated via suckers (86, 100), or other local adaptations, to expand operational range based on various sensing modalities (101).

Once grasped, an object can be manipulated by activating muscles at arm locations not in contact. For example, the arm of Fig. 5F uses its proximal section to bring the object to the opposite side, by relaxing its R-OM at the base before contracting its L-OM. To release the object, muscles are relaxed, letting passive elasticity loosen the grip. Passive elasticity can also mediate object transport. In Fig. 5G, an LM relaxation wavefront ( $\text{J}_\perp$ ) travels out from the base, transporting the object along. Indeed, as the longitudinal muscles relax, the arm uncurls while the initially injected curvature becomes increasingly localized in the distal section (Fig. 5H), allowing the arm to maintain its grasp.

Octopuses regularly probe and reach through small crevices to retrieve objects of interest (17, 102). We conclude by combining the lessons learned so far to enable a similar behavior in our model (Fig. 6 A and B). Motion is initiated by injecting a

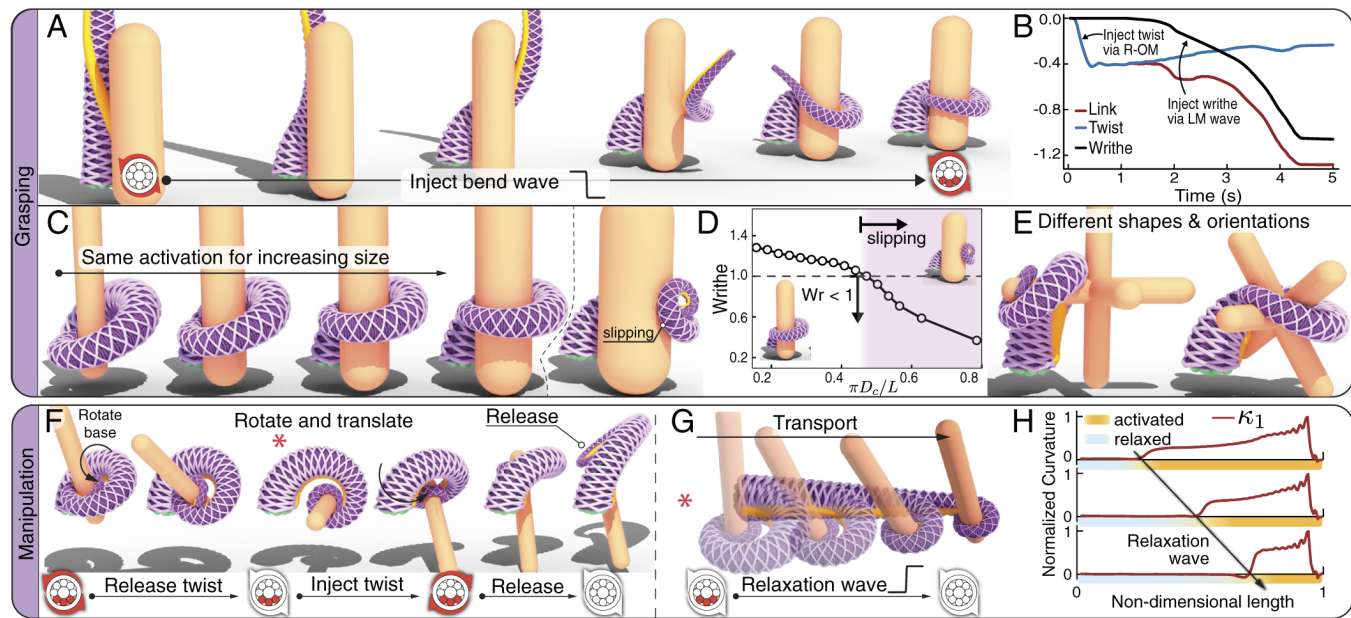


**Fig. 5.** Grasping and manipulation. (A) Grasping an object by injecting twist into the base and coiling via a bending wave. (B) Evolution of link, writhe, and twist of the arm during grasping motion. (C) The same muscle activation pattern successfully grasps cylinders of increasing diameter (Movie S4). (D) Writhe in an arm of length  $L$  grasping objects of diameter  $D_c$ . When  $|W_r| \lesssim 1$  the arm begins to slip (pink region). (E) The same muscle activation of (A) also allows the arm to grasp objects of different shapes and orientations. (F) A grasped object is manipulated by sequentially releasing R-OM and activating L-OM at the base to transport to the other side before being released via muscle relaxation (Movie S5). (G) The arm from (F), in the configuration denoted by the red star, transports the obstacle away from the base via an LM wave of relaxation (Movie S5). (H) As the relaxation wave travels toward the tip, the arm's passive elasticity straightens the arm, and bending curvature ( $\kappa_1$ ) becomes localized, maintaining grip.

bending wave from the base, as in Fig. 4B, although this time the proximal portion of the longitudinal muscles remains contracted to maintain the arm positioned toward the opening (steps ①–③). As the arm attempts to reach through, it encounters the obstacles that define the opening, however, thanks to its compliance, this disturbance is passively accommodated for, with the distal end of the arm deforming out of plane to slip past the solid boundary (④–⑥). Note that so far the suckers have been exposed outward (LM active on the same side), as typically observed in octopuses (17, 55). As the arm makes its way across the crevice, twist is injected to align the arm's suckers with the target (⑦) for grasping, which is enacted by bending the distal end via localized LM contractions on the suckers' side (⑧ and ⑨). Once grasped, the injected twist is released, rotating both arm and object by  $180^\circ$  (⑩–⑫) before all longitudinal muscles in the proximal and medial regions are contracted. This shortening primitive pulls the arm back out through the opening to extract the target despite obstacle collisions (⑬ and ⑭), which are passively dealt with. Notably, this entire motion sequence is accomplished by composing only three actuation primitives (bending wave, twisting, and shortening), with spatiotemporal profiles reported in Fig. 6B.

**Discussion.** By combining medical imaging and biomechanical data with rod-based modeling of heterogeneous, fibrous structures, the uniquely complex architecture of the octopus arm, and the mechanical program it embodies, is analyzed through the lens of topology and geometry. A control framework for grasping and manipulation is revealed, kinematically replicating prototypical 3D motions. It is important to remark that the modeling approach and topological control analysis presented here are not exclusive to octopuses. Rather, they are generally applicable to slender soft organs, from elephant trunks (22) to prehensile tongues (1, 80). Gleaned insights advance not only

our understanding of muscular hydrostats, providing testable hypotheses, but also inform translatable ‘mechanical intelligence’ principles to design and control future soft robots that seek to match the dexterity of their natural counterparts. Finally, this work is significant in terms of modeling from medical imaging, where rod-based approaches specialized to musculoskeletal systems promise patient-specific care opportunities.

## Materials and Methods

**Animal Care and Imaging.** Three adult female wild-caught *O. rubescens* were used in this study: one for histology imaging, one for MRI, and one for behavioral experiments. They were collected by Monterey Abalone, Inc. by trapping and shipped overnight to the University of Illinois in Urbana, IL. Animals were housed individually in temperature-controlled ( $12^\circ\text{C}$ ) glass aquaria enriched with clay-pot dens and fed a steady diet of diced squid. All animal procedures were in compliance with ARRIVE guidelines regulating animal experimentation. All efforts were made to minimize animal suffering and to reduce the number of animals used.

For imaging, two octopuses were anesthetized in seawater with 333 nM  $\text{MgCl}_2$  concentration. An arm was amputated from each. All procedures carried out complied with institutional recommendations for cephalopods. After surgery and recovery from anesthesia, live animals were replaced in their recirculating cold-water tanks ( $12^\circ\text{C}$ ) and monitored for signs of stress while healing. Animals accepted food at 2 d postsurgery and continued recovering well. The ex vivo tissues were placed in Tris-buffered sea water bath ( $18^\circ\text{C}$ ) for experimental procedures. Arms were fixed in 4% PFA for 48 h ( $4^\circ\text{C}$ ). For histology imaging, the arm was segmented into blocks along the cross-sectional and frontal planes, sectioned, and stained with hematoxylin and eosin to reveal the anatomical organization of the muscle fibers. Slides were imaged using a Nanoozometer 2.0-HT Slide Scanner. For MRI, the fixed arm was transferred to a  $1 \times$  PBS solution and 24 h prior to imaging the arm was placed in a tube with 15 mL of PBS and a  $4 \mu\text{L/mL}$  gadolinium concentration. T2-weighted and DTI scans were performed with a 9.4T Bruker preclinical scanner and a surface receive coil. The slice direction was aligned with the arm's axial orientation. For T2-

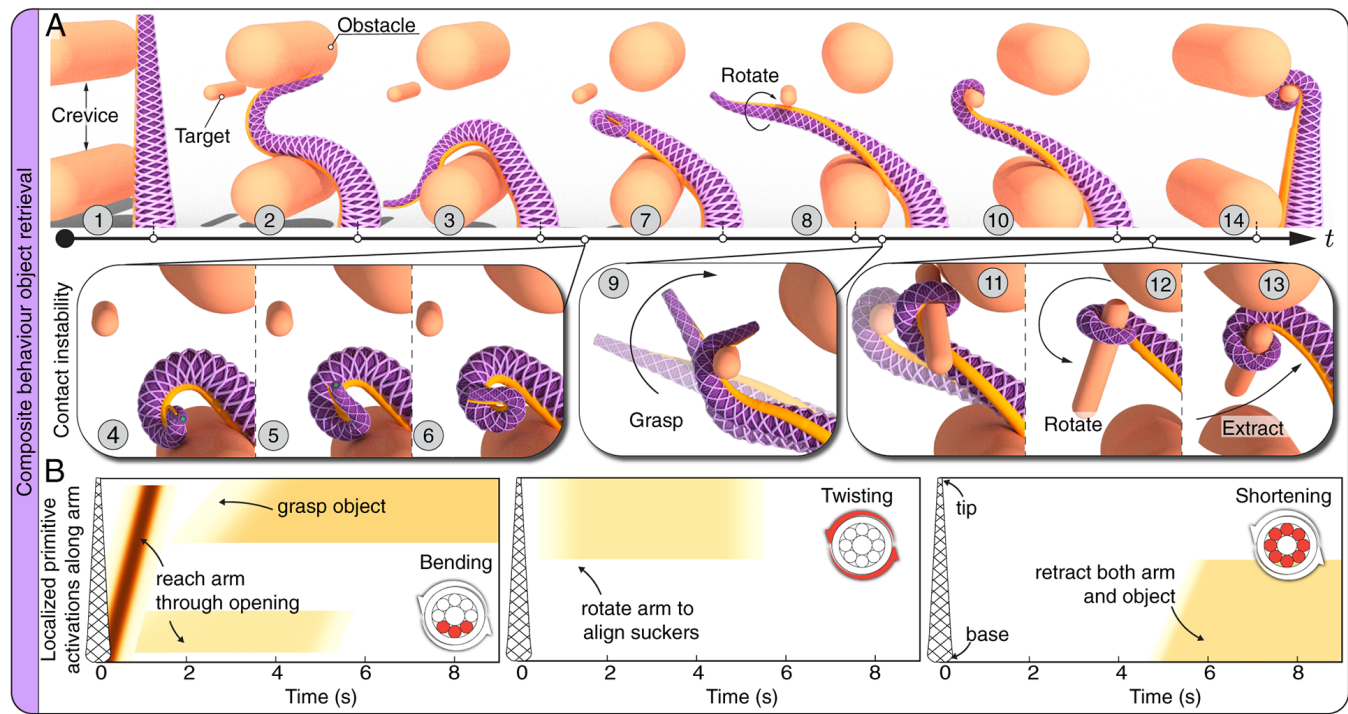


**Fig. 6.** Composite behavior: object retrieval. (A) An arm reaching through a crevice to grasp a target object. Insets: (steps 4–6) the arm's compliance accommodates imperfect reaching and solid obstacles by buckling out of plane; (step 7) grasping of the target; (steps 11–13) retrieval of the object where compliance again corrects for imprecise control (Movie S6). (B) Spatiotemporal activation maps for (A).

weighted scans, a TURBO RARE sequence was acquired over a 20 mm FOV with a  $256 \times 256$  matrix (78.125  $\mu\text{m}$  in-plane resolution), 20 slices (1 mm thickness), and TE/TR = 32/2,500 ms. DTI scans were acquired for a  $128 \times 128$  matrix (156.25  $\mu\text{m}$  resolution), 20 slices (1 mm), TE/TR = 32/1500 ms, 4 segments, 3 b-values of 500, 1,000, and 1,500  $\text{s/mm}^2$ , 12 directions, and 16 averages. Fiber tractography was performed using DSI Studio (103) over an ROI manually defined to isolate the arm.

**Arm Behavior Characterization from Video Recordings.** To characterize the modes of deformations employed by an octopus arm when manipulating objects, multiple trials of an *O. rubescens* interacting with objects were filmed. To isolate arm behaviors for recording, the octopus was placed in a clear acrylic box with a 9.5 mm diameter hole in the lower corner (sized to allow only 1 to 2 arms to reach through). Two objects of different shapes were presented outside the box near the hole and the octopus was allowed to freely reach through the hole and interact with them. A description of the objects is provided in SI Appendix, Supplementary Method 1. Videos were recorded using a Sony Alpha a7III camera at 30 fps with either 1080p or 4k resolution. Trials were performed over several days with 23 independent interactions with each object acquired. Videos were trimmed to isolate periods over which the arm was observed to interact with the object, and individual frames were extracted every 5 s, resulting in 691 frames for analysis. To quantify the deformation modes that emerge from the combination of muscular actuation, sucker adhesion, and environmental interactions, the shape of the arm was characterized based on the static poses visible in these frames. Adopting a scoring methodology similar to Kennedy et al. (16) and Grasso (97), we considered deformations over the proximal, medial, and distal sections of the arm. For each section, the arm's pose was categorized as one-dimensional (straight), two-dimensional (planar bending or coiling), or three-dimensional (helical or multiplane bending). A detailed description of the categorization protocol and statistical analysis of the observed motions is provided in SI Appendix, Supplementary Method 1. Example clips of the acquired videos are available in Movie S1.

**Modeling of an Octopus-Inspired Soft Arm.** We model our octopus-inspired soft arm as an assembly of Cosserat rods, which are slender, one-dimensional

elastic structures that can undergo all modes of deformation: bending, twisting, stretching, and shearing while conserving volume. Representing an octopus arm's different muscle groups as Cosserat rods entails a number of advantages as, assembled together, they naturally capture the heterogeneity of muscular architectures. Further, the Cosserat formulation can be extended to account for nonlinear material properties, connectivity, active stresses, internal pressure, and environmental loads. The numerical implementation of Cosserat rods is computationally efficient as they accurately capture large deformations in 3D space through a one-dimensional representation, alleviating time-consuming meshing difficulties and compute costs of 3D elasticity.

**Dynamics of a single Cosserat rod.** An individual Cosserat rod is described by its center line position  $\bar{x}(s, t) \in \mathbb{R}^3$  and an oriented reference frame of (row-wise) orthonormal directors  $\mathbf{Q}(s, t) \in \mathbb{R}^{3 \times 3} = [\bar{\mathbf{d}}_1, \bar{\mathbf{d}}_2, \bar{\mathbf{d}}_3]^{-1}$  along its length  $s \in [0, L(t)]$ , where  $L(t)$  is the current length, for all time  $t \in \mathbb{R} \geq 0$

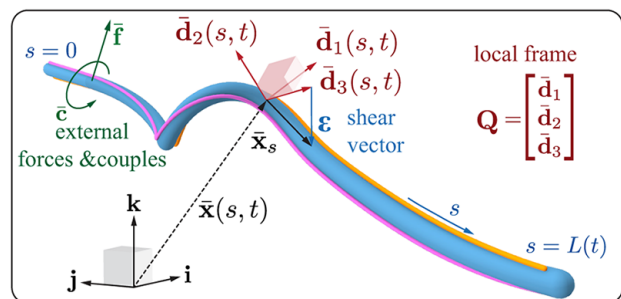


**Fig. 7.** Cosserat rod model: a Cosserat rod in three-dimensional space is described by a centerline  $\bar{x}(s, t)$  and a local frame  $\mathbf{Q}(s, t) = [\bar{\mathbf{d}}_1, \bar{\mathbf{d}}_2, \bar{\mathbf{d}}_3]^{-1}$ . Both are functions of rod's arc-length  $s$  and time  $t$ . The shear vector  $\epsilon$  quantifies the deviation of  $\bar{\mathbf{d}}_3(s, t)$  from the rod's tangent  $\bar{x}_s(s, t)$ . The elastic rod is deformed by external forces  $\mathbf{f}(s, t)$  and couples  $\mathbf{c}(s, t)$ . Yellow and pink lines trace out the orientation of  $\bar{\mathbf{d}}_1(s, t)$  and  $-\bar{\mathbf{d}}_1(s, t)$  along the rod, respectively.

(Fig. 7). Any vector defined in the global *lab frame* ( $\bar{\mathbf{v}}$ ) can be transformed into the *local frame* ( $\mathbf{v}$ ) via  $\mathbf{v} = \mathbf{Q}\bar{\mathbf{v}}$  and from the local to the lab frame via  $\bar{\mathbf{v}} = \mathbf{Q}^T\mathbf{v}$ . For an unshearable and inextensible rod,  $\bar{\mathbf{d}}_3$  is parallel to the rod's local tangent ( $\partial_s \bar{\mathbf{x}} = \bar{\mathbf{x}}_s$ ), and  $\bar{\mathbf{d}}_1$  (normal) and  $\bar{\mathbf{d}}_2$  (binormal) span the rod's cross-section. However, under shear or extension, the rod's tangent direction  $\bar{\mathbf{x}}_s$  and  $\bar{\mathbf{d}}_3$  are no longer the same, with the difference represented by the shear strain vector  $\boldsymbol{\epsilon} = \mathbf{Q}(\bar{\mathbf{x}}_s - \bar{\mathbf{d}}_3)$ . The gradient of the directors ( $\bar{\mathbf{d}}_j$ ) with respect to the rod's length is defined by the curvature vector  $\bar{\mathbf{k}}(s, t) \in \mathbb{R}^3$  through the relation  $\partial_s \bar{\mathbf{d}}_j = \bar{\mathbf{k}} \times \bar{\mathbf{d}}_j$ . In the local frame ( $\boldsymbol{\kappa} = \mathbf{Q}\bar{\mathbf{k}}$ ), the components of the curvature vector  $\boldsymbol{\kappa} = [\kappa_1, \kappa_2, \kappa_3]$  relate to bending ( $\kappa_1$  and  $\kappa_2$ ) and twisting ( $\kappa_3$ ) of the rod. Similarly, the gradient of the directors with respect to time is defined by the angular velocity vector  $\bar{\boldsymbol{\omega}}(s, t) \in \mathbb{R}^3$  through the relation  $\partial_t \bar{\mathbf{d}}_j = \bar{\boldsymbol{\omega}} \times \bar{\mathbf{d}}_j$ . The linear velocity of the centerline is  $\bar{\mathbf{v}}(s, t) \in \mathbb{R}^3 = \partial_t \bar{\mathbf{x}}$  while the second area moment of inertia  $\mathbf{I}(s, t) \in \mathbb{R}^{3 \times 3}$ , cross-sectional area  $A(s, t) \in \mathbb{R}$ , and density  $\rho(s) \in \mathbb{R}$  are defined based on the rod's material properties. The dynamics of a Cosserat rod are then described as (63)

$$\partial_t^2 (\rho A \bar{\mathbf{x}}) = \partial_s (\mathbf{Q}^T \mathbf{n}) + \bar{\mathbf{f}}, \quad [2]$$

$$\partial_t (\rho \mathbf{l} \boldsymbol{\omega}) = \partial_s \boldsymbol{\tau} + \boldsymbol{\kappa} \times \boldsymbol{\tau} + (\mathbf{Q} \bar{\mathbf{x}}_s \times \mathbf{n}) + (\rho \mathbf{l} \boldsymbol{\omega}) \times \boldsymbol{\omega} + \mathbf{Q} \bar{\mathbf{c}}, \quad [3]$$

where Eqs. 2 (lab frame) and 3 (local frame) represent the linear and angular momentum balance at every cross-section, respectively,  $\mathbf{n}(s, t) \in \mathbb{R}^3$  and  $\boldsymbol{\tau}(s, t) \in \mathbb{R}^3$  are internal forces and couples, respectively, developed due to elastic deformations and muscle contractions while  $\bar{\mathbf{f}}(s, t) \in \mathbb{R}^3$  and  $\bar{\mathbf{c}}(s, t) \in \mathbb{R}^3$  capture external forces and couples applied to the arm, respectively.

For a material with linear stress-strain behavior, the internal forces  $\mathbf{n} = [n_1, n_2, n_3]$  are proportional to the shear strain of the rod  $\mathbf{n} = \mathbf{S}(\boldsymbol{\epsilon} - \boldsymbol{\epsilon}_0)$ , where  $\boldsymbol{\epsilon}_0$  is the intrinsic shear strain of the rod,  $\mathbf{S} = \text{diag}(\alpha_c G A, \alpha_c G A, EA)$  is the rod's shear/stretch stiffness matrix,  $E$  is the rod's Young's modulus,  $G$  is the rod's shear modulus, and  $\alpha_c$  is the Timoshenko shear correction factor (63). Octopus muscles, however, exhibit nonlinear stress-strain relations in both their passive response to stretch and their ability to actively generate force. To account for this material behavior, we directly modify the axial stretch component ( $n_3$ ) of the internal force vector  $\mathbf{n}$  (described in the next section) while modeling its shear components ( $n_1, n_2$ ) using the above presented linear elastic formulation. Internal torques are modeled as  $\boldsymbol{\tau} = \mathbf{B}(\boldsymbol{\kappa} - \boldsymbol{\kappa}_0)$ , where  $\boldsymbol{\kappa}_0$  is the intrinsic curvature of the rod,  $\mathbf{B} \in \mathbb{R}^{3 \times 3} = \text{diag}(El_1, El_2, Gl_3)$  is the rod's bend/twist stiffness matrix, and  $l_1, l_2$ , and  $l_3$  are the rod's second moments of inertia about  $\bar{\mathbf{d}}_1, \bar{\mathbf{d}}_2$ , and  $\bar{\mathbf{d}}_3$ , respectively. To ensure incompressibility, the cross-section of each discretized rod element is dynamically rescaled according to its axial stretch (63). This causes both  $A$  and  $I$  to cease to be constant, resulting in a nonlinear relation between force-strain and torque-strain and enabling the Cosserat rod formulation to capture nonlinear material behaviors similar to the Neo-Hookean model (63), commonly used to model biological tissue. We also emphasize that the influence of the octopus muscle model extends to encompass angular momentum via the third term in Eq. 3. Material and geometric properties for the different muscle groups are based on experimental measurements and are provided in SI Appendix, Supplementary Method 2.

The above continuous representation is discretized into ( $n_{\text{elem}} + 1$ ) nodes of position  $\bar{\mathbf{x}}_i$  that are connected by  $n_{\text{elem}}$  cylindrical elements. Linear displacements are determined by the internal and external forces acting at the nodes, while rotations are accounted for via couples applied to the cylindrical elements. The dynamic behavior of a rod is computed by integrating the discretized set of equations, along with appropriate boundary conditions, in time via a second-order position Verlet scheme (63). Energy losses due to internal friction and viscoelastic effects are captured using a combination of Rayleigh potentials and Laplacian filters (described in SI Appendix). This numerical approach has been validated against a number of benchmark problems with known analytic solutions as well as experimental investigations involving contact, anisotropic surface friction, and highly viscous fluids (63). In this study, we used PyElastica (66), an open-source, Python-based implementation of this numerical scheme that has previously been demonstrated in both engineering and biophysical contexts, from the design of soft and biohybrid robots (73, 75, 104)

to the modeling of musculoskeletal architectures, including snakes (68) and human biceps (65).

Biological muscles actively generate internal forces that cause them to axially contract while exhibiting hyperelastic passive behavior when stretched. Both effects render a linear treatment of the Cosserat rod's axial stretch inaccurate in the context of the octopus. A description of how we model the active and passive mechanics of octopus models is provided in SI Appendix, section 2.2.

**Assembling Cosserat rods into an octopus arm.** We assemble our octopus arm by arranging active and passive rods into a representative muscular architecture based on medical imaging. The arm in its rest configuration presents no muscle activation or residual stresses. Such residual stresses, while important to the specific capabilities and behaviors of octopus arms (78), are not critical to understanding the broad mechanical and dynamical principles of actively articulated soft arms considered here and so are set aside. However, their incorporation is straightforward. A description of the arm's geometry and parameters is provided in SI Appendix. To fix the base of the arm in place, zero-displacement boundary conditions are defined at the nodes of the LM and ANC nearest the base. We also define three classes of boundary conditions to capture the possible modes of interaction between neighboring rods. This mechanical connectivity enables the arm to translate the one-dimensional internal contraction forces generated by individual muscles into the three-dimensional dynamic motions of the arm as a whole. As a general strategy, we enforce "soft" interaction constraints through displacement-force (or torque) restoring relationships (65) as well as through the incorporation of an intramuscular pressure model (described below) to enforce the arm's near incompressibility. Notably, our connected assembly of rods allows the arm to deform its overall cross-sectional shape in response to external or internal loads.

To connect neighboring rods together, we implement distributed displacement-force boundary conditions to capture, at first-order, the response of the collagen connective tissue that surrounds and binds together the octopus' muscle groups (76). Details of how connections are geometrically defined, how contact between rods is modeled, and how intramuscular pressure effects are captured are available in SI Appendix, section 2.3.

**Environmental Interactions.** We consider two forms of interaction: contact with solid objects and fluid drag.

All external obstacles are modeled as fixed, rigid cylinders. Their interaction with the arm is represented through a combination of friction and contact boundary conditions applied to the outermost muscle fibers (oblique muscles), following the approach of Haff and Werner (105). A detailed description of the contact and friction model is provided in SI Appendix, section 2.1.5.

Fluid drag forces depend on the geometrical and surface properties of the arm, as well as the fluid properties and flow conditions. While the full resolution of hydrodynamic effects is beyond the scope of this work, we implement the simplified drag model approach by Yekutieli et al. (47). Detailed descriptions of the modeling approach used to capture the fluid drag forces are provided in SI Appendix, section 2.1.6.

**Knot Theory Calculations.** We compute link  $\mathcal{L}k$ , writhe  $\mathcal{W}r$ , and twist  $\mathcal{T}w$  of the octopus arm according to the methodology developed by Charles et al. (106) for knot theory calculations of open curves. This work showed that, while the Calugareanu–Fuller–White (CFW) theorem formally applies only to closed ribbons, if one extends the ends of an open curve outward, the CFW theorem holds to vanishingly small errors. We consider the arm as a discretized, directed curve defined by the open axial curve  $\bar{\mathbf{x}}_i(s, t)$  and an associated normal vector  $\bar{\mathbf{d}}_{1,i}(s, t)$  based on the location and orientation of the axial nerve cord. We extend this curve by appending straight, untwisted segments to the base and tip of the arm. At the base, the segment extends from  $\bar{\mathbf{x}}_0 + \alpha L \frac{\bar{\mathbf{x}}_0 - \bar{\mathbf{x}}_1}{|\bar{\mathbf{x}}_0 - \bar{\mathbf{x}}_1|}$  while at the tip the segment extends from  $\bar{\mathbf{x}}_n + \alpha L \frac{\bar{\mathbf{x}}_n - \bar{\mathbf{x}}_{n-1}}{|\bar{\mathbf{x}}_n - \bar{\mathbf{x}}_{n-1}|}$ , where  $\alpha > 1$  and  $L$  is the length of the rod. We empirically chose  $\alpha = 10^3$  to ensure deviation from the CFW was negligible ( $|\mathcal{L}k - (\mathcal{W}r + \mathcal{T}w)| \lesssim 10^{-6}$ ). From this point,  $\bar{\mathbf{x}}_i(s, t)$  will refer to this extended curve. Finally, we define an auxiliary curve  $\bar{\mathbf{r}}_i(s, t) = \bar{\mathbf{x}}_i(s, t) + r(s, t) \bar{\mathbf{d}}_{1,i}(s, t)$ , where  $r(s, t)$  is the local radius of the arm

(yellow line in Figs. 3B and 7; a curve corresponding with  $-\bar{d}_1(s, t)$  is shown in pink). For these discretized curves, we compute link as

$$\mathcal{L}k = \sum_{i=0}^{n+1} \sum_{j=0}^{n+1} \frac{1}{4\pi} \Omega_{ij}, \quad [4]$$

where  $\Omega_{ij}$  is the solid angle determined by curve segments  $\bar{x}_i(s, t)$  and  $\bar{x}_j(s, t)$ . The sum runs over  $n + 2$  for each curve, corresponding to  $n$  physical segments and two additional segments. Similarly, since writhe is the link of the curve with itself, the same approach is used to compute writhe with the solid angle  $\Omega_{ij}$  now referring to the angle between two curve segments  $\bar{x}_i(s, t)$  and  $\bar{x}_j(s, t)$ . Twist ( $\mathcal{T}w$ ) is the rotation of curve  $\bar{r}_i(s, t)$  around  $\bar{x}_i(s, t)$  given as

$$\mathcal{T}w = \frac{1}{2\pi} \sum_{i=1}^{n-1} \phi_i, \quad [5]$$

where  $\phi_i$  is the angle between  $\bar{r}_i(s, t)$  and  $\bar{x}_i(s, t)$  at each element  $i$ . See section S2 of Charles et al. (106) for complete details.

**Data, Materials, and Software Availability.** All histology, MRI data, and behavior experiment videos described in this paper are deposited in Figshare

1. W. M. Kier, K. K. Smith, Tongues, tentacles and trunks: The biomechanics of movement in muscular-hydrostats. *Zool. J. Linn. Soc.* **83**, 307–324 (1985).
2. T. Flash, L. Zullo, Biomechanics, motor control and dynamic models of the soft limbs of the octopus and other cephalopods. *J. Exp. Biol.* **226**, jeb245295 (2023).
3. Y. Pretorius et al., Why elephant have trunks and giraffe long tongues: How plants shape large herbivore mouth morphology. *Acta Zool.* **97**, 246–254 (2016).
4. J. Shoshani, Understanding proboscidean evolution: A formidable task. *Trends Ecol. Evol.* **13**, 480–487 (1998).
5. R. Pfeifer, J. Bongard, *How the Body Shapes the Way We Think: A New View of Intelligence* (MIT Press, 2006).
6. T. Wang et al., Mechanical intelligence simplifies control in terrestrial limbless locomotion. *Sci. Robot.* **8**, eadi2243 (2023).
7. N. T. Ulrich, "Grasping with mechanical intelligence," Master's thesis, Department of Computer and Information Science, University of Pennsylvania, Philadelphia, PA (1988).
8. R. K. Katzschmann, C. Della Santina, Y. Toshimitsu, A. Cicchi, D. Rus, "Dynamic motion control of multi-segment soft robots using piecewise constant curvature matched with an augmented rigid body model" in 2019 2nd IEEE International Conference on Soft Robotics (RoboSoft) (IEEE, 2019), pp. 454–461.
9. C. Della Santina, C. Duriez, D. Rus, Model-based control of soft robots: A survey of the state of the art and open challenges. *IEEE Control Syst. Mag.* **43**, 30–65 (2023).
10. M. Stolze, L. Chin, R. L. Truby, D. Rus, C. Della Santina, "Modelling handed shearing auxetics: Selective piecewise constant strain kinematics and dynamic simulation" in 2023 IEEE International Conference on Soft Robotics (RoboSoft) (IEEE, 2023), pp. 1–8.
11. C. Della Santina, R. K. Katzschmann, A. Cicchi, D. Rus, Model-based dynamic feedback control of a planar soft robot: Trajectory tracking and interaction with the environment. *Int. J. Rob. Res.* **39**, 490–513 (2020).
12. D. Rus, M. T. Tolley, Design, fabrication and control of soft robots. *Nature* **521**, 467–475 (2015).
13. D. Trivedi, C. D. Rahn, W. M. Kier, I. D. Walker, Soft robotics: Biological inspiration, state of the art, and future research. *Appl. Bionics Biomed.* **5**, 99–117 (2008).
14. S. Kim, C. Laschi, B. Trimmer, Soft robotics: A bioinspired evolution in robotics. *Trends Biotechnol.* **31**, 287–294 (2013).
15. W. Kier, J. Leeuwen, A kinematic analysis of tentacle extension in the squid *Loligo pealei*. *J. Exp. Biol.* **200**, 41–53 (1997).
16. E. Kennedy, K. C. Buresch, P. Boinapally, R. T. Hanlon, Octopus arms exhibit exceptional flexibility. *Sci. Rep.* **10**, 1–10 (2020).
17. J. N. Richter, B. Hochner, M. J. Kubo, Octopus arm movements under constrained conditions: Adaptation, modification and plasticity of motor primitives. *J. Exp. Biol.* **218**, 1069–1076 (2015).
18. S. Hanassy, A. Botvinnik, T. Flash, B. Hochner, Stereotypical reaching movements of the octopus involve both bend propagation and arm elongation. *Bioinspiration Biomimetics* **10**, 035001 (2015).
19. I. Zelman et al., Kinematic decomposition and classification of octopus arm movements. *Front. Comput. Neurosci.* **7**, 60 (2013).
20. K. K. Smith, The use of the tongue and hyoid apparatus during feeding in lizards (*Ctenosaura similis* and *Tupinambis nigropunctatus*). *J. Zool.* **202**, 115–143 (1984).
21. P. C. Wainwright, A. F. Bennett, The mechanism of tongue projection in chameleons: II. Role of shape change in a muscular hydrostat. *J. Exp. Biol.* **168**, 23–40 (1992).
22. P. Dagenais, S. Hensman, V. Haechler, M. C. Milinkovitch, Elephants evolved strategies reducing the biomechanical complexity of their trunk. *Curr. Biol.* **31**, 4727–4737 (2021).
23. A. K. Schulz et al., Elephant trunks use an adaptable prehensile grip. *Bioinspiration Biomimetics* **18**, 026008 (2023).
24. J. Wu et al., Elephant trunks form joints to squeeze together small objects. *J. R. Soc. Interface* **15**, 20180377 (2018).
25. Y. Gutfreund, T. Flash, G. Fiorito, B. Hochner, Patterns of arm muscle activation involved in octopus reaching movements. *J. Neurosci.* **18**, 5976–5987 (1998).
26. G. Sumbre, Y. Gutfreund, G. Fiorito, T. Flash, B. Hochner, Control of octopus arm extension by a peripheral motor program. *Science* **293**, 1845–1848 (2001).
27. G. Sumbre, G. Fiorito, T. Flash, B. Hochner, Motor control of flexible octopus arms. *Nature* **433**, 595–596 (2005).
28. G. Sumbre, G. Fiorito, T. Flash, B. Hochner, Octopuses use a human-like strategy to control precise point-to-point arm movements. *Curr. Biol.* **16**, 767–772 (2006).
29. G. Bao et al., Trunk-like soft actuator: Design, modeling, and experiments. *Robotica* **38**, 732–746 (2020).
30. C. Laschi et al., Soft robot arm inspired by the octopus. *Adv. Rob.* **26**, 709–727 (2012).
31. I. D. Walker et al., "Continuum robot arms inspired by cephalopods" in *Unmanned Ground Vehicle Technology VII* (International Society for Optics and Photonics, 2005), vol. 5804, pp. 303–314.
32. R. Kang et al., Embodiment design of soft continuum robots. *Adv. Mech. Eng.* **8**, 1687814016643302 (2016).
33. R. V. Martinez et al., Robotic tentacles with three-dimensional mobility based on flexible elastomers. *Adv. Mater.* **25**, 205–212 (2013).
34. M. Wehner et al., An integrated design and fabrication strategy for entirely soft, autonomous robots. *Nature* **536**, 451–455 (2016).
35. M. Calisti et al., An octopus-bioinspired solution to movement and manipulation for soft robots. *Bioinspiration Biomimetics* **6**, 036002 (2011).
36. Y. Liu, Z. Ge, S. Yang, I. D. Walker, Z. Ju, Elephant's trunk robot: An extremely versatile under-actuated continuum robot driven by a single motor. *J. Mech. Rob.* **11**, 051008 (2019).
37. N. D. Naclerio et al., Controlling subterranean forces enables a fast, steerable, burrowing soft robot. *Sci. Robot.* **6**, eabe2922 (2021).
38. F. Connolly, C. J. Walsh, K. Bertoldi, Automatic design of fiber-reinforced soft actuators for trajectory matching. *Proc. Natl. Acad. Sci. U.S.A.* **114**, 51–56 (2017).
39. C. De Pascali, S. Palagi, B. Mazzolai, 3D-printed hierarchical arrangements of actuators mimicking biological muscular architectures. *Bioinspiration Biomimetics* **18**, 046014 (2023).
40. C. Laschi, B. Mazzolai, M. Ciachetti, Soft robotics: Technologies and systems pushing the boundaries of robot abilities. *Sci. Rob.* **1**, eaah3690 (2016).
41. P. Wang et al., Design and experimental characterization of a push-pull flexible rod-driven soft-bodied robot. *IEEE Rob. Autom. Lett.* **7**, 8933–8940 (2022).
42. Z. Xie et al., Soft robotic arm with extensible stiffening layer. *IEEE Rob. Autom. Lett.* **8**, 3597–3604 (2023).
43. C. Laschi, R. J. Wood, Smarter materials for smarter robots. *Sci. Robot.* **6**, eab94443 (2021).
44. J. Van Leeuwen, W. M. Kier, Functional design of tentacles in squid: Linking sarcomere ultrastructure to gross morphological dynamics. *Philos. Trans. R. Soc. Lond. B, Biol. Sci.* **352**, 551–571 (1997).
45. H. J. Chiel, P. Crago, J. M. Mansour, K. Hathi, Biomechanics of a muscular hydrostat: A model of lapping by a reptilian tongue. *Biol. Cybern.* **67**, 403–415 (1992).
46. Y. Liang, R. McMeeking, A. Evans, A finite element simulation scheme for biological muscular hydrostats. *J. Theor. Biol.* **242**, 142–150 (2006).
47. Y. Yekuteli et al., Dynamic model of the octopus arm. I. Biomechanics of the octopus reaching movement. *J. Neurophysiol.* **94**, 1443–1458 (2005).
48. B. Kaczmarski, A. Goriley, E. Kuhl, D. E. Moulton, A simulation tool for physics-informed control of biomimetic soft robotic arms. *IEEE Rob. Autom. Lett.* **8**, 936–943 (2023).
49. H. S. Chang et al., Energy-shaping control of a muscular octopus arm moving in three dimensions. *Proc. R. Soc. A* **479**, 20220593 (2023).
50. G. Mengaldo et al., A concise guide to modelling the physics of embodied intelligence in soft robotics. *Nat. Rev. Phys.* **4**, 595–610 (2022).
51. D. M. Kaufman, R. Tamstorf, B. Smith, J. M. Aubry, E. Grinspun, Adaptive nonlinearity for collisions in complex rod assemblies. *ACM Trans. Graph. (TOG)* **33**, 1–12 (2014).
52. M. Bergou, B. Audoly, E. Vouga, M. Wardetzky, E. Grinspun, Discrete viscous threads. *ACM Trans. Graph. (TOG)* **29**, 1–10 (2010).
53. J. Chang, F. Da, E. Grinspun, C. Batty, A unified simplicial model for mixed-dimensional and non-manifold deformable elastic objects. *Proc. ACM Comput. Graph. Interactive Tech.* **2**, 1–18 (2019).

(<https://figshare.com/s/cfd0ae1eaaf852ed630bf>) (105). Selected clips of object manipulation by the octopus and videos of the octopus arm model's dynamic motions are also provided in *SI Appendix*. Code for the octopus arm model presented here is available in *SI Appendix* and will be made available on GitHub upon publication (<https://github.com/GazzolaLab/PyElastica/tree/master>) (106).

**ACKNOWLEDGMENTS.** This study was jointly funded by ONR MURI N00014-19-1-2373 (M.G., P.G.M., and R.G.), ONR N00014-22-1-2569 (M.G.), NSF EFRI C3 SoRo #1830881 (M.G.), NSF CAREER #1846752 (M.G.), NSF EXPEDITION #IIS-2123781 (M.G.), and NSF IOS-1755231 (W.K.).

Author affiliations: <sup>a</sup>Mechanical Science and Engineering, University of Illinois Urbana-Champaign, Urbana, IL 61801; <sup>b</sup>Beckman Institute for Advanced Science and Technology, University of Illinois Urbana-Champaign, Urbana, IL 61801; <sup>c</sup>Coordinated Science Laboratory, University of Illinois Urbana-Champaign, Urbana, IL 61801; <sup>d</sup>Department of Molecular and Integrative Physiology, University of Illinois Urbana-Champaign, Urbana, IL 61801; <sup>e</sup>Department of Biology, University of North Carolina, Chapel Hill, NC 27599; <sup>f</sup>Carl R. Woese Institute for Genomic Biology, University of Illinois Urbana-Champaign, Urbana, IL 61801; and <sup>g</sup>National Center for Supercomputing Applications, University of Illinois Urbana-Champaign, Urbana, IL 61801

Author contributions: A.T., N.N., and M.G. designed research; A.T., N.N., S.H.K., and M.G. performed research; A.T., N.N., and M.G. analyzed data; and A.T., N.N., S.H.K., U.H., R.G., P.G.M., W.K., and M.G. wrote the paper.

54. H. S. Chang *et al.*, "Energy shaping control of a cyberoctopus soft arm" in 2020 59th IEEE Conference on Decision and Control (CDC), A. Aghdam, Ed. (Institute of Electrical and Electronics Engineers (IEEE), Jeju Island, Republic of Korea, 2020), pp. 3913–3920.
55. T. Wang *et al.*, "A sensory feedback control law for octopus arm movements" in 2022 IEEE 61st Conference on Decision and Control (CDC), A. Aghdam, Ed. (Institute of Electrical and Electronics Engineers (IEEE), Cancún, Mexico, 2022), pp. 1059–1066.
56. C. H. Shih *et al.*, Hierarchical control and learning of a foraging cyberoctopus. *Adv. Intell. Syst.* **5**, 2300088 (2023).
57. F. Renda, M. Cianchetti, M. Giorelli, A. Arienti, C. Laschi, A 3D steady-state model of a tendon-driven continuum soft manipulator inspired by the octopus arm. *Bioinspiration Biomimetics* **7**, 025006 (2012).
58. F. Ling, E. Kanso, "Octopus-inspired arm movements" in *Bioinspired Sensing, Actuation, and Control in Underwater Soft Robotic Systems*, D. A. Paley, N. M. Wereley, Eds. (Springer International Publishing, Cham, Switzerland, 2021), pp. 213–228.
59. A. Doroudchi, S. Berman, "Configuration tracking for soft continuum robotic arms using inverse dynamic control of a Cosserat rod model" in 2021 IEEE 4th International Conference on Soft Robotics (RoboSoft), R. Kramer-Bottiglio, Ed. (Institute of Electrical and Electronics Engineers (IEEE), New Haven, CT, 2021), pp. 207–214.
60. S. Shivakumar *et al.*, "Decentralized estimation and control of a soft robotic arm" in *Bioinspired Sensing, Actuation, and Control in Underwater Soft Robotic Systems*, D. A. Paley, N. M. Wereley, Eds., (Springer International Publishing, Cham, Switzerland, 2021), pp. 229–246.
61. S. S. Blemler, In vivo imaging of skeletal muscle form and function: 50 years of insight. *J. Biomech.* **158**, 111745 (2023).
62. L. Zullo, A. Di Clemente, F. Maiole, How octopus arm muscle contractile properties and anatomical organization contribute to arm functional specialization. *J. Exp. Biol.* **225**, jeb243163 (2022).
63. M. Gazzola, L. Dudte, A. McCormick, L. Mahadevan, Forward and inverse problems in the mechanics of soft filaments. *R. Soc. Open Sci.* **5**, 171628 (2018).
64. S. S. Antman, *Nonlinear Problems of Elasticity* (Springer, New York, NY, 1995).
65. X. Zhang, F. K. Chan, T. Parthasarathy, M. Gazzola, Modeling and simulation of complex dynamic musculoskeletal architectures. *Nat. Commun.* **10**, 1–12 (2019).
66. A. Tekinalp *et al.*, GazzolaLab/PyElastica (v0.3.2, 2023). <https://doi.org/10.5281/zenodo.10883271>. Accessed 26 March 2024.
67. A. Tekinalp, Y. Bhosale, S. Cui, F. K. Chan, M. Gazzola, Soft, slender and active structures in fluids: Embedding Cosserat rods in vortex methods. arXiv [Preprint] (2024). <https://arxiv.org/abs/2401.09506> (Accessed 17 January 2024).
68. X. Zhang, N. Naughton, T. Parthasarathy, M. Gazzola, Friction modulation in limbless, three-dimensional gaits and heterogeneous terrains. *Nat. Commun.* **12**, 1–8 (2021).
69. N. Charles, R. Chelakkot, M. Gazzola, B. Young, L. Mahadevan, Non-planar snake gaits: From stigmatic-starts to sidewinding. arXiv [Preprint] (2023). <https://arxiv.org/abs/2303.15482> (Accessed 5 April 2023).
70. A. Porat, A. Tekinalp, Y. Bhosale, M. Gazzola, Y. Meroz, On the mechanical origins of waving, coiling and skewing in *Arabidopsis thaliana* roots. *Proc. Natl. Acad. Sci. U.S.A.* **121**, e2312761121 (2024).
71. Y. Bhosale *et al.*, Micromechanical origin of plasticity and hysteresis in nestlike packings. *Phys. Rev. Lett.* **128**, 198003 (2022).
72. N. Weiner, Y. Bhosale, M. Gazzola, H. King, Mechanics of randomly packed filaments—the “bird nest” as meta-material. *J. Appl. Phys.* **127**, 050902 (2020).
73. N. Naughton *et al.*, Elastica: A compliant mechanics environment for soft robotic control. *IEEE Rob. Autom. Lett.* **6**, 3389–3396 (2021).
74. Y. Kim *et al.*, Remote control of muscle-driven miniature robots with battery-free wireless optoelectronics. *Sci. Rob.* **8**, eadd1053 (2023).
75. J. Wang *et al.*, Computationally assisted design and selection of maneuverable biological walking machines. *Adv. Intell. Syst.* **3**, 2000237 (2021).
76. W. M. Kier, M. P. Stella, The arrangement and function of octopus arm musculature and connective tissue. *J. Morphol.* **268**, 831–843 (2007).
77. L. Margheri, G. Ponte, B. Mazzolai, C. Laschi, G. Fiorito, Non-invasive study of *Octopus vulgaris* arm morphology using ultrasound. *J. Exp. Biol.* **214**, 3727–3731 (2011).
78. A. Di Clemente, F. Maiole, I. Bornia, L. Zullo, Beyond muscles: Role of intramuscular connective tissue elasticity and passive stiffness in octopus arm muscle function. *J. Exp. Biol.* **224**, jeb242644 (2021).
79. J. T. Thompson, K. R. Taylor-Burt, W. M. Kier, One size does not fit all: Diversity of length-force properties of obliquely striated muscles. *J. Exp. Biol.* **226**, jeb244949 (2023).
80. K. K. Smith, K. A. Mackay, The morphology of the intrinsic tongue musculature in snakes (Reptilia, Ophidia): Functional and phylogenetic implications. *J. Morphol.* **205**, 307–324 (1990).
81. S. Mori, P. C. Van Zijl, Fiber tracking: Principles and strategies—A technical review. *NMR Biomed.* **15**, 468–480 (2002).
82. T. A. Gaige, T. Benner, R. Wang, V. J. Wedeen, R. J. Gilbert, Three dimensional myoarchitecture of the human tongue determined in vivo by diffusion tensor imaging with tractography. *J. Magn. Reson. Imaging* **26**, 654–661 (2007).
83. F. B. Fuller, Decomposition of the linking number of a closed ribbon: A problem from molecular biology. *Proc. Natl. Acad. Sci. U.S.A.* **75**, 3557–3561 (1978).
84. H. Matzner, Y. Gutfreund, B. Hochner, Neuromuscular system of the flexible arm of the octopus: Physiological characterization. *J. Neurophysiol.* **83**, 1315–1328 (2000).
85. P. Jereb, C. F. Roper, *Cephalopods of the World—An Annotated and Illustrated Catalogue of Cephalopod Species Known to Date. Vol 2. Myopsid and Oegopsid Squids* (FAO, 2010), No. 2.
86. Z. Xie *et al.*, Octopus arm-inspired tapered soft actuators with suckers for improved grasping. *Soft Rob.* **7**, 639–648 (2020).
87. S. Fossati, F. Benfenati, L. Zullo, Morphological characterization of the *Octopus vulgaris* arm. *Vie Milieu* **1980** (61), 191–195 (2011).
88. W. R. Bauer, F. H. Crick, J. H. White, Supercoiled DNA. *Sci. Am.* **243**, 118–133 (1980).
89. G. Calugareanu, L'intégrale de gauss et l'analyse des noeuds tridimensionnels. *Rev. Math. Pures Appl.* **4**, 257–273 (1959).
90. G. van der Heijden, M. Peletier, R. Planqué, On end rotation for open rods undergoing large deformations. *O. Appl. Math.* **65**, 385–402 (2007).
91. C. L. Huffard, F. Boneka, R. J. Full, Underwater bipedal locomotion by octopuses in disguise. *Science* **307**, 1927 (2005).
92. P. Amadio, N. Josef, N. Sharshar, G. Fiorito, Bipedal locomotion in *Octopus vulgaris*: A complementary observation and some preliminary considerations. *Ecol. Evol.* **11**, 3679–3684 (2021).
93. S. L. O'Brien, C. O'Brien, First record of bipedal locomotion in *Callistoctopus furvus*. *J. Molluscan Stud.* **88**, eyac020 (2022).
94. C. L. Huffard, Locomotion by *Abdopus aculeatus* (Cephalopoda: Octopodidae): Walking the line between primary and secondary defenses. *J. Exp. Biol.* **209**, 3697–3707 (2006).
95. A. Packard, G. D. Sanders, Body patterns of *Octopus vulgaris* and maturation of the response to disturbance. *Anim. Behav.* **19**, 780–790 (1971).
96. J. A. Mather, J. S. Alupay, An ethogram for benthic octopods (Cephalopoda: Octopodidae). *J. Comp. Psychol.* **130**, 109 (2016).
97. F. W. Grasso, Octopus sucker-arm coordination in grasping and manipulation. *Am. Malacol. Bull.* **24**, 13–23 (2008).
98. Y. Gutfreund *et al.*, Organization of octopus arm movements: A model system for studying the control of flexible arms. *J. Neurosci.* **16**, 7297–7307 (1996).
99. M. Mantti, V. Cucucciolo, M. Cianchetti, Stiffening in soft robotics: A review of the state of the art. *IEEE Rob. Autom. Mag.* **23**, 93–106 (2016).
100. N. Sholl, A. Moss, W. M. Kier, K. Mohseni, A soft end effector inspired by cephalopod suckers and augmented by a dielectric elastomer actuator. *Soft Rob.* **6**, 356–367 (2019).
101. P. Ramdy, A. J. Ijspeert, The neuromechanics of animal locomotion: From biology to robotics and back. *Sci. Rob.* **8**, eadg0279 (2023).
102. J. N. Richter, B. Hochner, M. J. Kuba, Pull or push? Octopuses solve a puzzle problem *PLoS ONE* **11**, e0152048 (2016).
103. F. C. Yeh, T. D. Verstynen, Y. Wang, J. C. Fernández-Miranda, W. Y. I. Tseng, Deterministic diffusion fiber tracking improved by quantitative anisotropy. *PLoS ONE* **8**, e80713 (2013).
104. O. Aydin *et al.*, Neuromuscular actuation of biohybrid motile bots. *Proc. Natl. Acad. Sci. U.S.A.* **116**, 19841–19847 (2019).
105. P. K. Haff, B. T. Werner, Computer simulation of the mechanical sorting of grains. *Powder Technol.* **48**, 239–245 (1986).
106. N. Charles, M. Gazzola, L. Mahadevan, Topology, geometry, and mechanics of strongly stretched and twisted filaments: Solenoids, plectonemes, and artificial muscle fibers. *Phys. Rev. Lett.* **123**, 208003 (2019).
107. N. Naughton, A. Tekinalp, M. Gazzola, Imaging data for “Topology, dynamics, and control of a muscle-architected soft arm.” figshare. <https://doi.org/10.6084/m9.figshare.c.6480442.v1>. Deposited 26 August 2024.
108. A. Tekinalp, N. Naughton, S. H. Kim, M. Gazzola, GazzolaLab/topology-dynamics-control-of-a-muscle-architected-soft-arm. Zenodo. <https://doi.org/10.5281/zenodo.13689233>. Deposited 5 September 2024.